RSC Advances

ROYAL SOCIETY OF CHEMISTRY

PAPER

View Article Online
View Journal | View Issue

Cite this: *RSC Adv.*, 2022, **12**, 29845

Core-shell structured Co_3O_4@PPy composite for electrochemical determination of terbutylhydroquinone†

Yuxi Zhang,‡*[ab] Cunli Wang,‡[c] Yalin Zhao,[c] Zhe Yu,[c] Fengchun Yang *[bc] and Xin Zhang *[c]

Received 5th September 2022
Accepted 6th October 2022

DOI: 10.1039/d2ra05574k

rsc.li/rsc-advances

TBHQ is a significant synthetic antioxidant, but excessive use of TBHQ is harmful to human health. Therefore, the preparation of a high-efficiency TBHQ electrochemical sensor is of great significance. In this work, a core–shell structured Co_3O_4@PPy composite is synthesized for TBHQ determination and exhibits remarkable electrochemical properties. The core–shell structure of Co_3O_4@PPy composite shows the synergistic effects of fast charge transfer, rich active surface area and more active sites. Under optimal conditions, the linear range of the developed sensor is 0.2–600 μM, and the detection limit is 0.05 μM (S/N = 3). In addition, it also has good stability and reproducibility due to the stable protective role of the PPy shell. The proposed sensor can also be applied to practical sample detection.

Introduction

Terbutylhydroquinone (TBHQ) is a significant synthetic antioxidant for preventing oxidative degradation of oil and efficiently scavenging free radicals, thus plays a vital role in the food industry.[1,2] Unfortunately, excessive use of TBHQ leads to cell damage and carcinogenesis.[3,4] Many diseases related to the immune system are associated with excessive TBHQ concentration, such as visual impairment, contact dermatitis, and convulsions.[5–8] Therefore, there is a standardized regulation for TBHQ intake of less than 200 mg g^{-1} in many countries.[9] Currently, several approaches have been reported for determining TBHQ. Among them, the electrochemical method has been proven to be an ideal technique for monitoring TBHQ due to its high sensitivity, fast detection speed, convenient portability and easy miniaturization.[10,11]

Cobalt tetroxide (Co_3O_4) is considered to be the most active metal oxide catalyst with certain advantages, such as special chemical stability, large specific surface area and excellent surface redox performance.[12,13] Exposing redox reaction sites through rational design of the Co_3O_4 structure is regarded as a high-efficiency strategy to boost its electrochemical sensing performance. Recently, some studies report a promising strategy on enhancing the electrochemical activity of an electrode by coating with a conducting polymer, which can adapt to the structure change and increase the electrode stability.[14,15] Polypyrrole (PPy) is very suitable for an electrode material, with its high specific surface area, good flexibility and strong conductivity.[16,17] Especially, PPy does not destroy the basic structure of the substrate due to the gentle synthesis process, and can effectively as a shell layer on metal oxides increase electrochemical performance of the electrode materials.[18] Therefore, the combination of PPy and Co_3O_4 through a reasonable design is of great significance for TBHQ determination.

In this paper, a Co_3O_4@PPy composite with core–shell structure is successfully fabricated by a hydrothermal method and chemical oxidation method, which not only shows facilitated electron transfer and enriched reaction sites for a highly efficient determination of TBHQ owing to the synergistic effects of Co_3O_4 core and PPy shell. In addition, the PPy shell also increases the stability of the sensor. Considering the excellent properties of the prepared Co_3O_4@PPy electrochemical sensor, such as wide detection range, high sensitivity, good anti-interference, stability and repeatability, the core–shell structure can be a promising alternative for the determination of TBHQ.

Experimental

Reagents and apparatus

Cobalt nitrate ($Co(NO_3)_3 \cdot 6H_2O$) (≥98.5%), pyrrole (≥98%), polyvinylpyrrolidone (PVP) (M_w: 55 000), ammonium persulfate

---

[a] *The Institute of Hydrogeology and Environmental Geology, Chinese Academy of Geological Sciences, Shijiazhuang, Hebei, 050061, China. E-mail: zhangyuxi@mail.cgs.gov.cn*

[b] *Key Laboratory of Groundwater Contamination and Remediation, China Geological Survey & Hebei Province, Shijiazhuang, Hebei, 050061, China. E-mail: fyang@nwu.edu.cn*

[c] *Key Laboratory of Synthetic and Natural Functional Molecule Chemistry of Ministry of Education, College of Chemistry & Material Science, Northwest University, Xi'an 710127, China*

† Electronic supplementary information (ESI) available. See https://doi.org/10.1039/d2ra05574k

‡ Yuxi Zhang and Cunli Wang contributed equally.

(APS), terbutylhydroquinone (TBHQ) (≥98%), ethanol (C_2H_5OH) (≥99.7%), *N*,*N*-dimethylformamide (DMF) (≥99.5%), sodium hydrogen phosphate (Na_2HPO_4) (≥99.0%), sodium dihydrogen phosphate (NaH_2PO_4) (≥99.0%), potassium chloride (KCl) (≥99.0%) were purchased from Sinopharm Chemical Reagent Co., Ltd (Shanghai, China). Sodium *p*-toluenesulfonate ($C_7H_7SO_3Na$) (≥99.5%), concentrated sulfuric acid (H_2SO_4) (≥98.0%) were provided by Damao Chemical Reagent b (Tianjin, China). The deionized water was from a Millipore Autopure system (18.20 MΩ, Millipore Ltd, USA).

The morphology of various materials was observed *via* scanning electron microscopy (SEM, SU8010, Japan) and transmission electron microscopy (TEM, FEI Talos F200X, USA). The crystal phases were characterized by X-ray diffraction (XRD, Bruker Advance, Germany). The FT-IR spectra was obtained with a Fourier transform infrared spectroscopy (FT-IR, Bruker TENSOR 27, Germany). The Raman spectra was analyzed by Raman spectroscopy (Renishaw, U.K.) with a laser excitation of 532 nm. The X-ray photoelectron spectroscopy data were performed by X-ray photoelectron spectroscopy (XPS, Thermoelectricity Instruments, USA). The CHI 630E electrochemical workstation (Shanghai, China) was used to collect all electrochemical data.

Synthesis of Co_3O_4 microcubes

Co_3O_4 microcubes was prepared through a method previously reported in the literature. Briefly, $Co(NO_3)_3\cdot 6H_2O$ (145.5 mg) was dissolved in 15 mL mixed solution containing deionized (DI) water and ethanol (DI : ethanol = 1 : 1). Subsequently, 100 mg PVP was added into the above solution under stirring continuously for 30 min. Then, the prepared solution was transferred into autoclave and maintained at 180 °C for 12 h. After cooling to room temperature, the product was washed with water and ethanol several times and followed by drying at 60 °C for 12 h to obtain Co_3O_4 microcubes.[19]

Synthesis of Co_3O_4@PPy

Co_3O_4 (24 mg) and sodium *p*-toluenesulfonate (33.59 mg) were dispersed in 2 mL ethanol water in a volume ratio of 1 : 1. Sodium *p*-toluenesulfonate was introduced into the PPy chains to increase the conductivity of PPy.[20,21] Afterwards, 12 μL of pyrrole monomer was added into the above solution with stirring continuously for 30 minutes. Then, 3 mL of 28.53 mg mL^{-1} ammonium persulfate (APS) solution was added slowly under a magnetic stirring. After oxidation induced polymerization, the solution was stirred in ice-water bath for 3 h at low temperature.

Ultimately, the resultant product was centrifuged with ethanol and water for several times and dried in a vacuum at 60 °C to form Co_3O_4@PPy.[22]

Preparation of Co_3O_4@PPy/GCE

Glassy carbon electrode (GCE) was polished on a chamois with 0.05 μm alumina slurry, then was cleaned successively with dilute sulphuric acid, ethanol and double distilled deionized water by sonication. 2 mg of Co_3O_4@PPy composite was dispersed in 1 mL of DMF to attain homogeneous suspension. Then, 10 μL of the Co_3O_4@PPy suspension was dropped onto the GCE surface and the solvent was dried under an infrared lamp in order to remove or evaporate the solvent.

Electrochemical measurement

Cyclic voltammetry (CV) was used to investigate electrochemical properties in 0.1 M PBS solution from −0.4–0.6 V at a scan rate of 100 mV s^{-1}. Electrochemical impedance spectroscopy (EIS) was performed in a 5.0 mM $[Fe(CN)_6]^{3-/4-}$ solution containing 0.1 M KCl. Under the condition of the pulse width was 0.05, the pulse period was 0.5 and the quiet time was 2, differential pulse voltammetry (DPV) with the potential scanning range from −0.4 to 0.6 V was recorded to evaluate electrochemical performance of Co_3O_4@PPy electrodes.

Pretreatment of sesame blend oil

Sesame blend oil was purchased from local supermarkets and pretreated for TBHQ determination. In brief, the 5 mL sample of sesame blend oil was mixed with 10 mL ethanol under stirring continuously for half an hour. Then, the mixture was subjected to centrifugation at 8000 rpm for 10 min, and the supernatant was collected and extracted for three time. Finally, the obtained supernatant was stored in a refrigerator.

Results and discussion

Characterization of Co_3O_4@PPy

The preparation for Co_3O_4@PPy core shell-structured composite *via* two-steps method is illustrated in Fig. 1a. Firstly, Co_3O_4 is synthesized from cobalt nitrate solution containing PVP at 180 °C by hydrothermal routine, which has an extremely smooth surface and a perfect cubic shape with an average size of 500 nm, as shown in Fig. 1b. Afterwards, the as-synthesized Co_3O_4 microcubes are transferred into different volume of Py monomer solution (6 μL, 12 μL, 18 μL, 24 μL) for the surface polymerization.

The structures and morphologies of the as-fabricated Co_3O_4@PPy composites are respectively presented in Fig. S1a–S1d† and 1c. Their electrochemical properties are also evaluated in Fig. S2.† Apparently, a stable and higher redox couple is observed for Co_3O_4@PPy with 12 μL Py monomer. This may be attributed to the fact that the thickness of PPy has a great influence on the electrochemical properties of Co_3O_4@PPy composites. When a small amount of Py monomer is polymerized on the surface of Co_3O_4, Co_3O_4 could not be completely covered by PPy film. As the volume of Py increases, more PPy film with large specific surface area is polymerized on the surface of Co_3O_4, which can effectively improve the catalytic activity for the electro-oxidation of TBHQ. However, with the further increase of Py monomer volume, the excessively thicker PPy films on Co_3O_4 surface would not further increased effective surface area, but reduce the electron transfer efficiency and hinder the electro-oxidation of TBHQ.[23]

Fig. 1c shows the SEM morphology of the optimized Co_3O_4@PPy (12 μL), and its high-resolution SEM image shows Co_3O_4 is evenly wrapped by the PPy film with a size of about

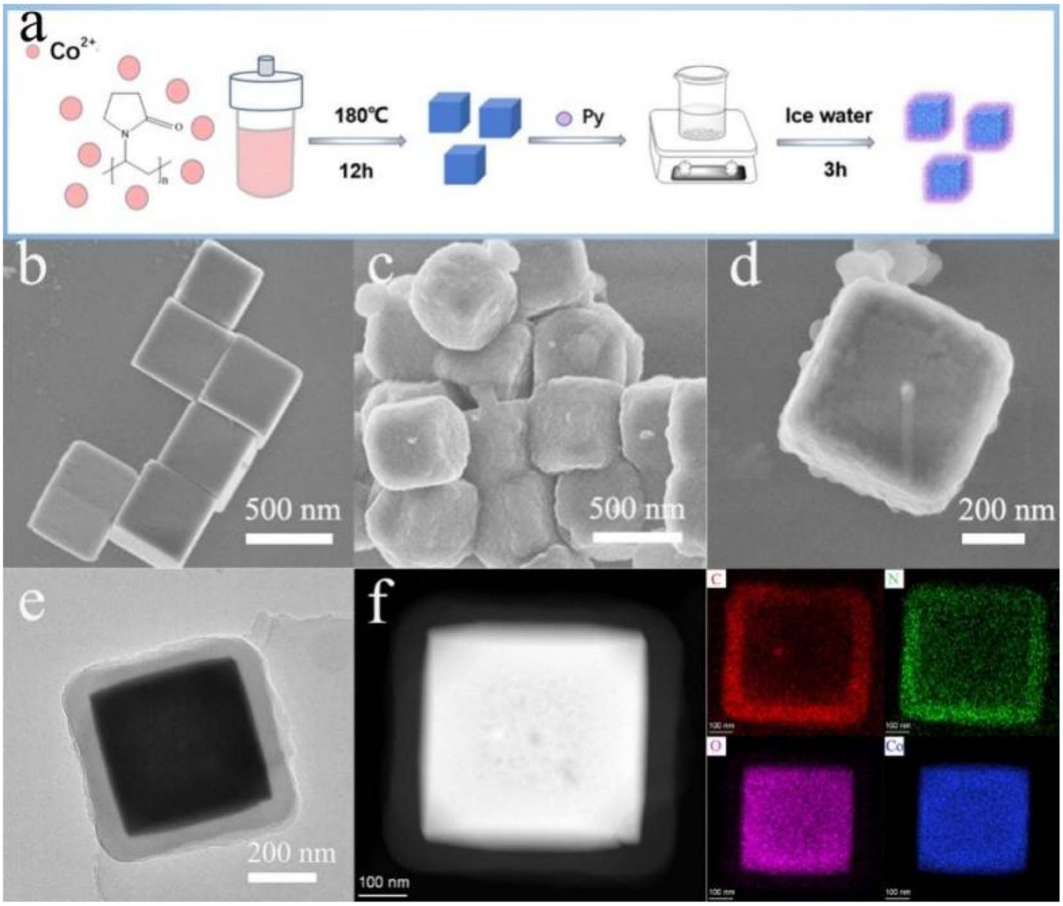

Fig. 1 (a) Schematic illustration of the formation of core–shell Co_3O_4@PPy. SEM images of (b) Co_3O_4 and (c) Co_3O_4@PPy. (d) High-resolution SEM image of Co_3O_4@PPy. (e) TEM images of Co_3O_4@PPy. (f) EDS-TEM elemental mapping of C, N, O, Co for Co_3O_4@PPy.

600 nm (Fig. 1d). The transmission electron microscopy (TEM) presents the internal structured morphology of Co_3O_4@PPy composite, and the thickness of PPy film is estimated to be about 50 nm (Fig. 1e). Energy dispersive X-ray spectroscopy (EDS) elemental mapping is conducted (Fig. 1f) to reveal the structure of the composites with the outer layer of PPy and the inner core of Co_3O_4, and confirm the formation of core–shell structured Co_3O_4@PPy.

The crystallographic structure of Co_3O_4 is shown in Fig. 2a, and the diffraction peaks are consistent with standard spinel Co_3O_4 (PDF#43-1003). After surface polymerization, a prominent intense peak at 23° is observed at the Co_3O_4@PPy composite, which is assigned to the presence of PPy.[24] Raman analysis is also employed to characterize the structure of the Co_3O_4@PPy (Fig. 2b). The peak at about 1583 cm^{-1} is assigned to symmetrical stretching vibration of aromatic C=C ring; the characteristic peaks at 1370 cm^{-1} and 1335 cm^{-1} are attributed to the ring stretching mode of PPy; the peak located at 1045 cm^{-1} is related to C–H in plane deformation. Notably, the peaks at 691 cm^{-1}, 523 cm^{-1} and 482 cm^{-1} belonging to Co_3O_4 (ref. 25–27) are greatly reduced after polymerization with PPy, which indicates the excellent encapsulation of PPy outside Co_3O_4, resulting in extremely weak peaks of Co_3O_4 that almost disappear. Fig. S3† displays FT-IR spectrum of as-prepared Co_3O_4@PPy, PPy and Co_3O_4, and the attribution of all peaks in FT-IR spectrum is listed in Table S1.†[28–34] It can be observed that the characteristic peaks of Co_3O_4 and PPy appear on the Co_3O_4@PPy composite, indicating the preparation of composite materials. All those characteristic results of XRD, Raman and FT-IR indicate that core–shell structured Co_3O_4@PPy is successfully prepared.

X-ray electron spectroscopy (XPS) is scrutinized to characterize the chemical composition and valence states of PPy, Co_3O_4 and Co_3O_4@PPy. Fig. S4† shows XPS survey spectrum of Co_3O_4@PPy, in which the C, N, O, Co elements can be detected. The peaks of C, O and N are high, while the Co peak is extremely weak, which indicates that there may be a small amount of incompletely encapsulated Co_3O_4 in the composite. Therefore, the Co 2p signal is still detected, which is also beneficial to investigate the electronic interactions between Co_3O_4 and PPy. Fig. 2c and d respectively show the N 1s and Co 2p XPS spectrum. After surface polymerization, the peak of N 1s shifts to lower binding energy, while the peak of Co_3O_4@PPy (Co 2p) moves towards higher binding energy. It shows that there is electron transfer from Co_3O_4 to PPy, which improves the coupling interaction between PPy and Co_3O_4, thus enhancing the efficiency of charge transfer. Additionally, Co donates electrons to the N position in PPy, giving Co_3O_4@PPy abundant

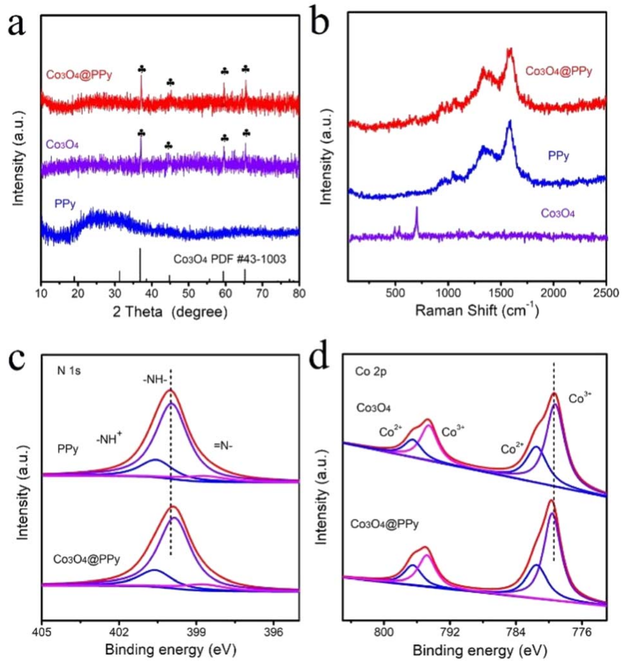

Fig. 2 (a) XRD patterns of Co_3O_4, PPy and Co_3O_4@PPy. (b) Raman spectrum of Co_3O_4, PPy and Co_3O_4@PPy. (c) High resolution N 1s XPS spectrum of PPy and Co_3O_4@PPy. (d) High resolution Co 2p XPS spectrum of Co_3O_4 and Co_3O_4@PPy.

electron delocalization centers and creating rich active sites in Co_3O_4@PPy.

Electrochemical properties of core–shell Co_3O_4@PPy

Electrochemical impedance spectroscopy (EIS) is implemented to investigate charge transport characteristics. In the high-frequency region, the semicircle part of the EIS diagram is related to electron transfer, while in the low-frequency region, the linear part represents the diffusion process. As shown in Fig. 3a, bare GCE, PPy, Co_3O_4, Co_3O_4@PPy exhibited decreasing in semicircle part gradually. Compared to other modified electrodes, the semicircle diameter of Co_3O_4@PPy is much smaller. This result proved that the modification of Co_3O_4 or PPy could reduce the resistances slightly, which could attributed to their own excellent conductivity. And the resistance drastically reduce after modification of Co_3O_4@PPy, demonstrating that the synergistic effects of Co_3O_4 and PPy further facilitated electron transfer. On the whole, Co_3O_4@PPy has smaller resistance and higher electron transfer ability.

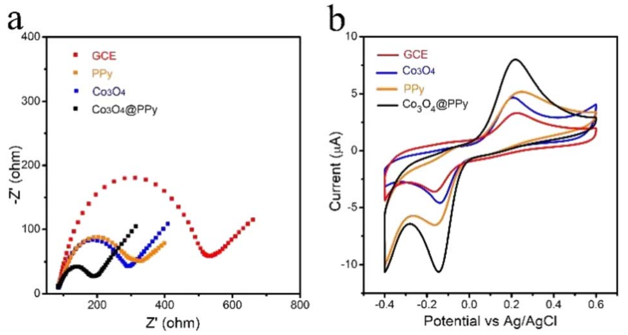

Fig. 3 (a) EIS of GCE, PPy, Co_3O_4, Co_3O_4@PPy in 5 mM $[Fe(CN)_6]^{3-/4-}$ solution containing 0.1 M KCl. (b) CVs of GCE, PPy, Co_3O_4, Co_3O_4@PPy containing 100 μM TBHQ in 0.1 M PBS solution (pH = 7).

The electrochemical responses of different electrodes for TBHQ (100 μM) in 0.1 M PBS (pH = 7) solution are examined by the CV, as shown in Fig. S5.† In the blank buffer solution, there are no redox peaks on Co_3O_4@PPy, Co_3O_4, PPy and GCE. However, after adding TBHQ, a pair of distinct redox peaks can be observed on all electrodes, which is clearly derived from the electro-redox of TBHQ. Fig. 3b compares the electrocatalytic oxidation of TBHQ on Co_3O_4@PPy, Co_3O_4, PPy and GCE. The small redox peak current of bare GCE is observed, showing poor electrocatalytic performance of bare GCE for TBHQ. After coated by Co_3O_4, the oxidation peak current of Co_3O_4/GCE increase slightly, which may be attributed to the high electrocatalytic capacity of Co_3O_4. However, after loading PPy, Co_3O_4@PPy electrode exhibits further increased peak current (6.15 μA), which is about 3-fold higher than bare GCE (1.98 μA). Besides, the response peak current increases linearly with the increase of TBHQ concentration from 0 to 250 μM (Fig. S6†). These results suggest that the Co_3O_4@PPy electrode has excellent synergistic effect of fast charge transfer, rich active surface area and more active sites, which are beneficial to achieve the effective determination of TBHQ.

Electrochemical reaction mechanism of TBHQ

The Co_3O_4@PPy sensing performance is evaluated by CV method with different buffer solution (HAc-NaAc, Na_2HPO_4-CA and PBS) and different pH (6.0–8.0) to find the optimal sensing platform. As shown in Fig. S7,† the highest current response is obtained in PBS buffer solution. This observation might be associated with higher migration rate of TBHQ in PBS, accelerating the electron transfer between the electrode and the solution.[35] As shown in Fig. 4a, the peak current increases from pH 6.0 to pH 7.0 and decreases progressively from pH 7.0 to pH 8.0. The strongest response is attained at pH 7.0 for TBHQ sensing (Fig. 4b). Thus, subsequent experiments are performed with an optimum pH of 7.0. Besides, the oxidation peak potential (E_{pa}) shifts linearly with the pH value, showing that protons are involved in the electrochemical reaction of TBHQ. According to the linear relationship between pH value and the anode peak potential, the regression equation is E_{pa} (V) = -0.064 pH + 0.686. The slope value is 64 mV pH^{-1}, which is consistent with the theoretical value of 0.059 V, suggesting that an equal number of protons and electrons transferred in the TBHQ oxidation process.[36]

The electrooxidation behavior of TBHQ in Co_3O_4@PPy is also explored by CV method with different scan rate to investigate the sensing mechanism (Fig. 4c). Obviously, the oxidation peak current (I_{pa}) of TBHQ increases gradually with the scan rate increasing in the range of 20–100 mV s^{-1}, and proportional to the linear relationship of I_{pa} (μA) = 1.548 + 48.62ν (Fig. 4d). The result reveals that typical adsorption-controlled process occurs on the Co_3O_4@PPy electrode. For adsorption-controlled

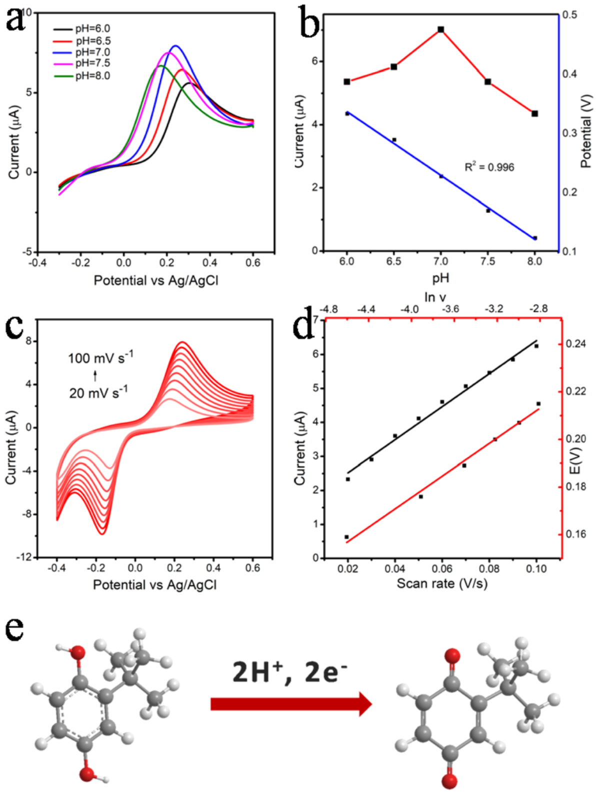

Fig. 4 (a) Positive voltammetry curves of 100 μM TBHQ at the Co_3O_4@PPy/GCE in 0.1 M PBS solution under different pH values (6.0–8.0). (b) The relationship between pH and peak potential E, and the effect of pH on the anodic peak current. (c) CVs of the Co_3O_4@PPy/GCE in 0.1 M PBS solution containing 100 μM TBHQ at different scan rates. (d) Corresponding calibration plot of I_p *vs.* ν and $E(V)$ *vs.* ln ν. (e) Electrochemical reaction mechanism diagram of TBHQ.

electrode process, E_p and ν is defined by the following equation according to Laviron's equation:[37]

$$E_p = E^0 + \frac{RT}{\alpha nF}\ln\left(\frac{RTk^0}{\alpha nF}\right) + \frac{RT}{\alpha nF}\ln \nu \qquad (1)$$

where α is the transfer coefficient, k^0 is the standard rate constant of the reaction, n is the electron transfer number, and E^0 is the formal potential. Therefore, n and α values can be easily obtained by eqn (1), respectively. Assuming that the value of α is 0.42, the value of n is calculated to be 2. Thus, two electrons have participated in the electrochemical oxidation of TBHQ. As mentioned above, an equal number of protons and electrons transferred in the TBHQ oxidation process. Therefore, the electrooxidation mechanism of TBHQ at Co_3O_4@PPy electrode may be proposed in Fig. 4e.

Analytical performance of Co_3O_4@PPy to TBHQ

Accumulation method is applied before determination to enhance the sensitivity. As shown in Fig. S8.† It is obviously observed that accumulation time and accumulation potential have a great impact on electrochemical sensing ability of the Co_3O_4@PPy electrode for TBHQ. Fig. S8a† shows the oxidation peak current has been increasing with accumulation time from 30 s to 90 s. However, the oxidation peak current increases slowly after 60 s, which may be because the adsorption capacity of TBHQ on the electrode has reached saturation with the increase of accumulation time. Based on this, 60 s is chosen as the best accumulation time. The influence of accumulation potential is also investigated in Fig. S8b.† Apparently, the maximum oxidation peak current is obtained at 0.1 V, which is determined as the best accumulation potential for TBHQ detection.

Differential pulse voltammetry (DPV) technique is used to investigate the electrooxidation responses of the Co_3O_4@PPy for TBHQ quantitative detection (Fig. 5a). With the increase of TBHQ concentration in the range of 0.2–600 μM, the oxidation peak current increases steadily with no significant shift in potential, showing good determination ability of TBHQ based on Co_3O_4@PPy. Fig. 5b describes the linear relationship between TBHQ concentration and oxidation peak current, and its linear equation are I_{pa} (μA) $= 0.00410 + 0.0569C$ ($R^2 = 0.992$) and I_{pa} (μA) $= 0.641 + 0.0100C$ ($R^2 = 0.996$). The sensitivity of the

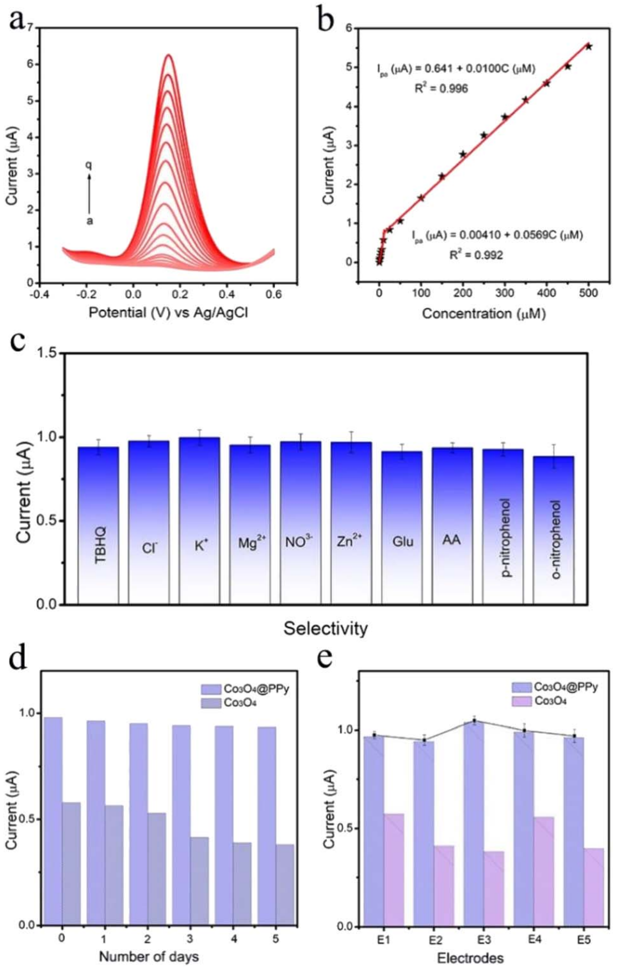

Fig. 5 (a) DPV of Co_3O_4@PPy composite at different concentrations. (b) The linear relationship between the corresponding peak current and TBHQ concentration. (c) Anti-interference of Co_3O_4@PPy/GCE. (d) Stability of Co_3O_4@PPy/GCE and Co_3O_4/GCE. (e) Repeatability of Co_3O_4@PPy/GCE and Co_3O_4/GCE.

first linear range is 0.803 μA μM^{-1} cm^2, and the sensitivity of the second linear range is 0.141 μA μM^{-1} cm^2. The decrease of sensitivity in the second linear range may be attributed to the fact that the active sites on the electrode surface tends to be saturated with the successively increasing TBHQ concentrations, which limits the adsorption control process of TBHQ.[38] According to the first linear equation, the detection limit (LOD) is calculated as 0.05 μM (S/N = 3). Table S2† lists other reported sensor for TBHQ determination, and the proposed sensor outperforms them in terms of wider linear range and lower LOD. Therefore, Co_3O_4@PPy electrode shows satisfactory capability toward TBHQ determination. The improved activity may be ascribed to the excellent electron transfer ability and increased active sites of core–shell structure composites, promoting the electrochemical chemical reaction kinetics.

Anti-interference, stability, reproducibility

Anti-interference study of Co_3O_4@PPy is performed by adding several potential interfering substances (Cl^-, K^+, Mg^{2+}, NO_3^-, Zn^{2+}, AA, Glu, *p*-nitrophenol and *o*-nitrophenol) to observe the effect on the TBHQ determination. Fig. 5c illustrates that the interferences have barely influence on the current response, and the as-prepared sensor has highly specific response toward TBHQ. The long-term stability is examined to evaluate current response of the Co_3O_4@PPy electrode for 5 days (Fig. 5d), and the current response remains 98% of the initial current after 5 days, proving the proposed sensor exhibits good stability.

For the reproducibility test, DPV is recorded by five times with Co_3O_4@PPy electrode under identical conditions. The results shows that the current response does not change significantly, and the RSD value of their peak current range from 1.2–3.6% (Fig. 5e), confirming admirable reproducibility of the proposed sensor. In addition, it can be observed from Fig. 5d and e that the stability of Co_3O_4@PPy composite is greatly improved compared with Co_3O_4 alone, which is mainly attributed to the existence of the shell buffer layer of PPy. The results prove that the PPy shell plays a key role in improving electrochemical stability, ensuring a longer service life for the Co_3O_4@PPy sensor.

Determination of TBHQ in real samples

Feasibility of the established sensor in determining practical samples is tested by assaying TBHQ in sesame blend oil *via* the standard addition method. A certain amount of TBHQ (50, 80, 100 μM) is added to the pretreated sesame oil, and the current response of the developed sensor in the actual sample is recorded, and the detailed information is listed in Table S3.† Its recoveries ranging from 99.0 to 101% and RSD value varying from 2.0% to 3.6% show satisfied accuracy of Co_3O_4@PPy in real sample determination, indicating the great potential in practical application.

Conclusion

Co_3O_4@PPy composite material with cored shell structure is synthesized for electrochemical determination of TBHQ, with wide detection range, low detection limit and good stability. The excellent sensing performance benefits from the strong coupling interaction of inner Co_3O_4 and outer PPy, which contribute to facilitate the electron transfer and create more active sites. In addition, the PPy shell is beneficial to increase the stability of the sensor. Thus, the proposed electrochemical sensor can also be applied for practical application. Considering the outstanding performance of the core–shell structure of Co_3O_4@PPy, this sensing platform will have a broad application prospect in the detection of other substances.

Author contributions

Yuxi Zhang: resources, funding acquisition, project administration. Cunli Wang: data curation, methodology, writing – original draft. Yalin Zhao: writing – review & editing. Zhe Yu: visualization. Fengchun Yang: supervision, funding acquisition. Xin Zhang: writing – review & editing, conceptualization, project administration.

Conflicts of interest

There are no conflicts to declare.

Acknowledgements

We gratefully acknowledge the support from the National Key R&D Program of China (grant number 2018YFC1803001), the National Natural Science Foundation of China (No. 21405120) and China Hydrogeological Survey Project of Huangshui River (No. DD20190331).

Notes and references

1 J. Tang, S. Zheng, S. Jiang, S. Jiang, J. Li, T. Guo and J. Guo, *Rare Met.*, 2021, **40**, 478–488.
2 N. Sebastian, W. Yu, D. Balram and S. Al-Mubaddel, *Food Chem.*, 2022, **377**, 131867.
3 M. Eskandani, H. Hamishehkar and J. Dolatabadi, *Food Chem.*, 2014, **153**, 315–320.
4 M. Wang, J. Wei, B. Tian B, J. Chen, Z. Wang and X. Pan, *Chem. Eng. J.*, 2022, **429**, 132169.
5 Y. Luo, Y. Yang, L. Wang and S. Chen, *J. Alloys Compd.*, 2022, **906**, 164369.
6 X. Yue, X. Luo, Z. Zhou and Y. Bai, *Food Chem.*, 2019, **289**, 84–94.
7 Z. Bin, L. Feng and Y. Yan, *Food Chem.*, 2022, **388**, 132898.
8 Y. Ma, J. Li and L. Wang, *Food Chem.*, 2021, **365**, 130462.
9 D. Balram, K. Lian, N. Sebastian and N. Rasanac, *J. Hazard. Mater.*, 2021, **406**, 124792.
10 Y. Wang, L. Wang, W. Huang, T. Zhang, X. Hu, A. Perman and S. Ma, *J. Mater. Chem. A*, 2017, **5**, 8385.
11 T. Kokulnathan, F. Ahmed, S. Chen, T. Chen, P. Hasan, A. Bilgrami and R. Darwesh, *ACS Appl. Mater. Interfaces*, 2021, **13**, 10987–10995.
12 D. Xu, J. Li and B. Li, *Chem. Eng. J.*, 2022, **434**, 134545.

13 Q. Guo, H. Song, M. Sun, H. Zhao, H. Zhu, J. Kou, F. Zhang, Z. Dong and J. Ma, *J. Hazard. Mater.*, 2022, **429**, 128193.
14 S. Zhang, Y. Jiang, H. Bai and J. Yang, *J. Phys. Chem. C*, 2020, **124**, 19467–19475.
15 M. Yan, Y. Yao, J. Wen, L. Long, M. Kong, G. Zhang, X. Liao, G. Yin and Z. Huang, *ACS Appl. Mater. Interfaces*, 2016, **8**, 24525–24535.
16 W. Yang, C. Weng, X. Li, H. He, J. Fei, W. Xu, X. Yan, W. Zhu, H. Zhang and X. Zhou, *Sens. Actuators, B*, 2021, **338**, 129844.
17 Q. Wang, Y. Ma, X. Liang, D. Zhang and M. Miao, *J. Mater. Chem. A*, 2018, **6**, 10361–10369.
18 Z. Fan, J. Zhu, X. Sun, Z. Cheng, Y. Liu and Y. Wang, *ACS Appl. Mater. Interfaces*, 2017, **9**, 21763–21772.
19 Y. Pan, H. Ren, H. Du, F. Cao, Y. Jiang, H. Dua and D. Chu, *J. Mater. Chem. A*, 2018, **6**, 22497–22502.
20 M. Zhang, A. Nautiyal, H. Du, J. Li, Z. Liu, X. Zhang and R. Wang, *Electrochim. Acta*, 2020, **357**, 136877.
21 Y. Huang, H. Li, Z. Wang, M. Zhu, Z. Pei, Q. Xue, Y. Huang and C. Zhi, *Nano Energy*, 2016, **22**, 422–438.
22 K. Ke, L. Lin, H. Liang, X. Chen, C. Han, J. Li and H. Yang, *Chem. Commun.*, 2015, **51**, 6800–6803.
23 Z. Xu, H. Teng and J. Song, *Microchim. Acta*, 2019, **186**, 1–8.
24 D. Zhang, Z. Wu, X. Zong and Y. Zhang, *Sens. Actuators, B*, 2018, **274**, 575–586.
25 U. Acharya, P. Bober and M. Trchová, *Polymers*, 2018, **150**, 130–137.
26 R. Oliveira, J. Milikić, E. Daş, A. Yurtcan, D. Santos and Ba. Šljukićab, *Appl. Catal., B*, 2018, **238**, 454–464.
27 M. Saghafi, M. Mahmoodian and S. Hosseini, *Electrochim. Acta*, 2018, **283**, 1450–1459.
28 X. Lian, W. Guo, Y. Wu, Y. Tian and S. Wang, *J. Alloys Compd.*, 2021, **865**, 158296.
29 Y. Chen, W. Huang, K. Chen, T. Zhang, Y. Wang and J. Wang, *Sens. Actuators, B*, 2019, **290**, 434–442.
30 C. Yang, B. Bai, Y. He, N. Hu, H. Wang and Y. Suo, *Ind. Eng. Chem. Res.*, 2018, **57**, 4955–4966.
31 J. Xu, Y. Hu, C. Zeng, Y. Zhang and H. Huang, *J. Colloid Interface Sci.*, 2017, **505**, 719–727.
32 T. Mokkelbost, I. Kaus and T. Grande, *Chem. Mater.*, 2004, **16**, 5489–5494.
33 V. Vatanpour, A. Ghadimi and A. Karimi, *Mater. Sci. Eng., C*, 2018, **89**, 41–51.
34 Y. Han, T. Wang and T. Li, *Carbon*, 2017, **119**, 111–118.
35 R. Carvalho, N. Yotsumoto and S. Carvalho, *Electroanalysis*, 2016, **28**, 2930–2938.
36 T. Gan, A. Zhao and S. Wang, *Sens. Actuators, B*, 2016, **235**, 707–716.
37 E. Laviron, *J. Electroanal. Chem. Interfacial Electrochem.*, 1974, **52**, 355–393.
38 Y. Wang, L. Wang and H. Chen, *ACS Appl. Mater. Interfaces*, 2016, **8**, 18173–18181.